
Training Like a Medical Resident: Universal Medical Image Segmentation via Context Prior Learning

Yunhe Gao¹Zhuowei Li¹Di Liu¹Mu Zhou¹Shaoting Zhang²Dimitris N. Metaxas¹¹Department of Computer Science, Rutgers University² Shanghai Artificial Intelligence Laboratory

Abstract

A major enduring focus of clinical workflows is disease analytics and diagnosis, leading to medical imaging datasets where the modalities and annotations are strongly tied to specific clinical objectives. To date, building task-specific segmentation models is intuitive yet a restrictive approach, lacking insights gained from widespread imaging cohorts. Inspired by the training of medical residents, we explore universal medical image segmentation, whose goal is to learn from diverse medical imaging sources covering a range of clinical targets, body regions, and image modalities. Following this paradigm, we propose *Hermes*¹, a context prior learning approach that addresses the challenges related to the heterogeneity on data, modality, and annotations in the proposed universal paradigm. In a collection of seven diverse datasets, we demonstrate the appealing merits of the universal paradigm over the traditional task-specific training paradigm. By leveraging the synergy among various tasks, *Hermes* shows superior performance and model scalability. Our in-depth investigation on two additional datasets reveals *Hermes*' strong capabilities for transfer learning, incremental learning, and generalization to different downstream tasks. The code is available².

1 Introduction

Medical image segmentation offers the detailed delineation of anatomical structures that is crucial for disease diagnosis [10, 45] and treatment planning [39, 15, 14]. To date, the prevailing training paradigm for medical image segmentation revolves around developing separate models for specific medical objects (e.g., organs or tumors) and image modalities (e.g., CT or MR) [24, 17]. This paradigm is often constrained by the limited data from the same domain, resulting in compromised robustness and generalizability of models. Further scaling up data volumes for specific segmentation tasks is challenging due to the high cost of data acquisition, collection, and annotation [42]. Moreover, the current paradigm fails to exploit potential relationships among medical imaging tasks. These limitations together confine the capability and scalability of medical image segmentation models.

By observing the training program of radiology residency, we recognize that radiologists' expertise arises from routine exposure to a diverse range of medical images across body regions, diseases, and imaging modalities. During this process, essential prior knowledge about the target regions of interest (ROI) and their visual features across imaging modalities is gained for interpreting the subtle patterns. Inspired by this observation, it is intuitive to train a universal segmentation model from

¹We name our approach after *Hermes*, a multifaceted deity in Greek mythology, symbolizing the versatility and the oracle-guided learning of prior knowledge it employs.

²<https://github.com/yhygao/universal-medical-image-segmentation>

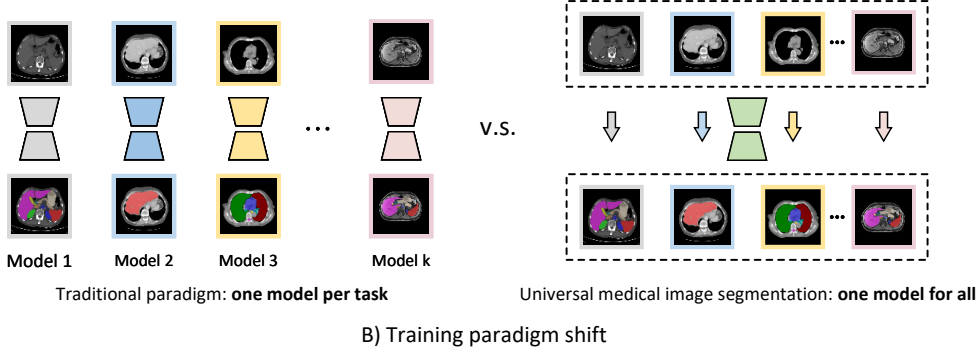
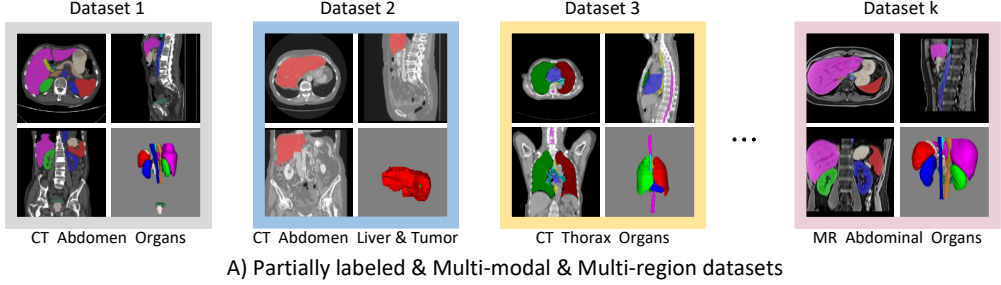


Figure 1: A) Clinical diagnostic workflows typically focus on specific specialties and diseases, leading to the curation of image datasets that are partially annotated, multi-modal, and multi-regional. B) Traditional training paradigms involve training separate models for each segmentation task (or dataset). In this study, we emphasize a universal medical image segmentation paradigm aiming at **one model for all**, leading to a robust and generalizable universal model for diverse tasks.

diverse sources of medical images. However, addressing the significant heterogeneity among medical imaging tasks faces daunting challenges.

Firstly, each image dataset has different and even incomplete ROI annotations, due to their distinct needs and clinical objectives. As seen in Figure 1, dataset 1 contains annotations for 15 abdominal organs, while dataset 2 is annotated for the liver and tumor only. Secondly, class definitions can vary depending on the clinical target. To illustrate, in dataset 1, the liver is annotated as a whole organ, whereas in dataset 2, the same liver region is divided into two categories: liver and tumor. Additionally, images from different datasets exhibit significant statistical divergence due to factors such as imaging modalities (dataset k) and body regions (dataset 3).

Given these challenges, several intriguing questions remain to be explored. Can tasks with different target regions of interest mutually benefit from each other? Is the underlying representation transferable across different body regions? Despite the visual difference of imaging modalities, can a model discern and utilize the commonalities between them?

In this paper, we attempt to answer the above questions. Our main contributions are:

- We introduce and explore the universal medical image segmentation paradigm, whose goal is training a universal model that learns *transferable* and *generalizable* representation from diverse image sources, covering various ROIs, anatomical regions, and imaging modalities.
- We propose Hermes to address the substantial heterogeneity in universal medical image segmentation. To mimic the medical training of radiology residency, Hermes explicitly learns a context prior knowledge pool consisting of task and modality information, along with the segmentation backbone. By using the assigned target regions of interest and image modality as oracles, Hermes can inject the corresponding prior knowledge to enhance model segmentation performance.
- By carefully curating seven datasets to train Hermes, our systematic analysis answers the above questions and reveals the strong capability of Hermes in universal medical image segmentation with regard to performance and model scalability.

- Through two additional downstream datasets, Hermes demonstrates superior performance in transfer learning, incremental learning, and generalization, affirming the efficacy of the universal medical image segmentation paradigm in acquiring robust and generalizable image representations.

2 Related Works

Partially labeled data problem. Clinical workflows have an enduring focus on the analysis of disease-specific imaging modalities. This results in the wide presence of single-modality images and partial annotations only tied to specific clinical objectives. Existing research such as Conditional CNN [11] has shown the feasibility of multi-class segmentation using models trained on single-class datasets. Incorporating domain-specific knowledge [54] is helpful by regularizing organ size distribution, but it relies on specific optimization techniques. Alternatively, multi-organ pseudo labels can be generated from multiple single-organ models and then co-training a unified model [23]. Recent studies have addressed the partially labeled data problem by conditioning the model’s output on certain inputs. DoDNet [51] employed dynamic filtering conditioned on a one-hot embedded task vector for organ and tumor segmentation. Recent CLIP-driven universal model [34] demonstrates its promise, where the model’s output is conditioned on the task information embedded by the CLIP text encoder. However, their method was limited as CLIP’s text encoder is rarely trained on medical text data, and couldn’t effectively encode the semantics of medical objects. While addressing partial labeling, these works limit their data to a single body region or imaging modality. In contrast, our focus is placed on learning from diverse data sources, encompassing different body regions, modalities, and target ROIs.

In-context learning and multi-task learning. In-context learning can execute multiple tasks via a few input-label demonstrations in large language models (LLM) [4, 53, 33], and has been extended to vision tasks [48]. Research indicates that LLMs implicitly infer tasks from demonstrations [49, 9, 38]. However, in medical image segmentation, the necessary context information is already provided before human interpretation, eliminating the need for model inference. For example, we have already known which objects require segmentation (the tasks), and the image modality information is stored as meta-data within the image header file. As a result, we propose leveraging these known factors as “oracles” to guide the explicit learning of context priors as model input conditions, rather than inferring them during testing. We introduce two types of context priors: *task* and *modality*, implemented as learnable tokens inspired by [26]. Our work is also influenced by multi-task learning [44] and meta-training [37, 13], emphasizing that learning from a large collection of tasks can result in improved performance and adaptability to unseen tasks.

Universal image segmentation aims to unify semantic, instance, and panoptic segmentation into one framework [52, 8, 7]. However, in 3D medical imaging, it is uncommon to find multiple instances of the same object. In addition, fully annotated medical datasets are rarely available in the community, making instance and panoptic segmentation highly unsuitable. As a result, universal medical image segmentation focuses on the semantic segmentation of medical objects. While sharing similarities, developing universal medical image segmentation possesses unique challenges, including the presence of partial annotation, conflicting class definitions, and heterogeneous medical-image contents [42].

3 Method

3.1 Preliminary

Problem definition. We hereby define *universal medical image segmentation* as the endeavor to train a universal model that learns from diverse medical datasets and performs various image segmentation tasks. Given a set of K datasets, let $\mathcal{D}_k = \{(\mathbf{x}_k^i, \mathbf{y}_k^i, m_k, \mathbf{t}_k)\}_{i=1}^{N_k}$ be the k -th dataset comprised of N_k data pairs, where each data pair $(\mathbf{x}_k^i, \mathbf{y}_k^i) \in (\mathcal{X}_k \times \mathcal{Y}_k)$. m_k denotes the image modality of \mathcal{D}_k and \mathbf{t}_k represents the tasks contained in \mathcal{D}_k , where each task represents the segmentation of a unique clinical target annotated in \mathcal{Y}_k , and $|\mathbf{t}_k| = |\mathcal{Y}_k|$. The collective dataset is given by $\mathcal{D} = \cup_{k=1}^K \mathcal{D}_k$, the corresponding collective tasks are $\mathcal{T} = \cup_{k=1}^K \mathbf{t}_k$, and the collective modalities are $\mathcal{M} = \cup_{k=1}^K m_k$. The objective is to train a single model $f_\theta : \mathcal{X} \rightarrow \mathcal{Y}$, parameterized by θ , where $\mathcal{X} = \cup_{k=1}^K \mathcal{X}_k$ and $\mathcal{Y} = \cup_{k=1}^K \mathcal{Y}_k$.

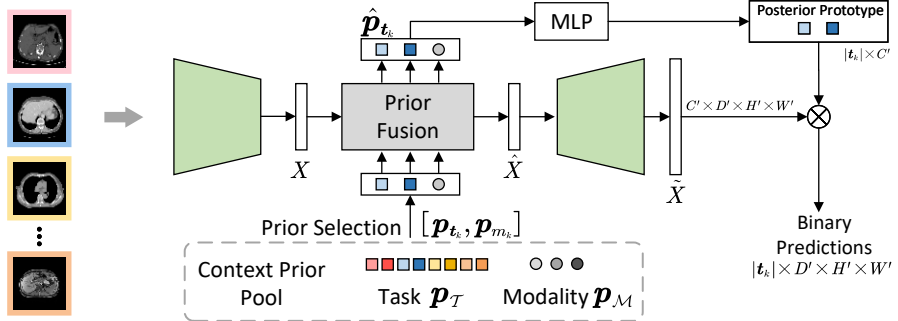


Figure 2: Illustration of Hermes. A context prior knowledge pool, including task and modality priors, is learned with the segmentation backbone. Through oracle-guided selection and combination of these priors, Hermes can address a variety of segmentation tasks and image modalities.

3.2 Oracle-guided context prior learning

In this section, we introduce Hermes, an oracle-guided context prior learning approach, as depicted in Fig. 2. Drawing inspiration from radiology residency training, Hermes explicitly learns context prior knowledge along with the segmentation backbone from diverse medical imaging sources. In line with radiologists’ practice for image interpretation, Hermes uses the tasks to be processed t , and the imaging modality m as guiding oracles during inference. These oracles guide the selection and combination of two types of priors - *task* and *modality* - to aid the backbone in addressing any specified tasks from the collective dataset. As a model-agnostic approach, Hermes can be seamlessly integrated with existing segmentation backbones, offering a versatile solution for universal medical image segmentation.

Task context prior. To learn from varied datasets and handle the incomplete annotation and potential conflict of class definition, each task in \mathcal{T} is formed as a binary segmentation task. For example, if ROIs in different datasets share the exact same definition, they are considered a single task, otherwise are treated as separate tasks. Each task is associated with a unique task prior, which is implemented as a learnable token. For the collective dataset \mathcal{D} comprising $|\mathcal{T}|$ tasks, we initialize a task prior pool $\mathbf{p}_{\mathcal{T}} \in \mathbb{R}^{|\mathcal{T}| \times C}$, where C denotes the token dimension. Given a training image from \mathcal{D}_k , we use the task IDs t_k as an oracle to guide the selection of corresponding task priors $\mathbf{p}_{t_k} \in \mathbb{R}^{|t_k| \times C}$ from the pool, on which the model are conditioned to complete specified tasks. This design enables Hermes to flexibly select and combine task priors based on clinical objectives, accommodating a wide array of medical segmentation tasks.

Conditioned segmentation. Given an encoded feature map $X \in \mathbb{R}^{C \times D \times H \times W}$ from the segmentation backbone, where D, H, W represent the 3D feature map sizes, a prior fusion module is applied to adaptively fuse task context prior tokens and image features:

$$\hat{\mathbf{p}}_{t_k}, \hat{X} = \text{Fusion}(\mathbf{p}_{t_k}, X). \quad (1)$$

Here, $\hat{\mathbf{p}}_{t_k}$ and \hat{X} represent the posterior token and prior-injected feature map, respectively. The prior fusion module can be implemented with the attention mechanism. For CNN backbones, we employ bi-directional cross-attention modules. For Transformer, we merge the prior tokens into the attention module (detailed in the appendix). The posterior tokens are then processed by a multilayer perceptron (MLP) module to obtain the posterior prototypes, which are used as classifiers for the corresponding classes. The predicted probability distribution for each task is computed as the inner product between the posterior prototypes and image features followed by a sigmoid function:

$$\hat{y} = p_{\theta}(y_k = 1 | \mathbf{x}, \mathbf{p}_{t_k}) = \sigma(\langle \hat{\mathbf{p}}_{t_k}, \tilde{X} \rangle) \quad (2)$$

where $\hat{\mathbf{p}}_{t_k} \in \mathbb{R}^{|t_k| \times C'}$ represents the posterior prototypes (overload the $\hat{\mathbf{p}}_{t_k}$ in equation (1)), $\tilde{X} \in \mathbb{R}^{C' \times D' \times H' \times W'}$ denotes the output feature map of the decoder, and the prediction $\hat{y} \in \mathbb{R}^{|t_k| \times D' \times H' \times W'}$ is the predicted probability for tasks t_k .

Intuitively, each task prior token learns the representation for its corresponding class from the entire dataset during training. At inference, the task priors are updated based on the observations by aggregating knowledge from the feature maps. This update is weighted by the attention weights between the task priors and the feature map, resulting in an instance-specific posterior prototype for segmentation. Above designs render Hermes a dynamic and adaptive inference process, thereby boosting the segmentation performance.

Modality context prior. Medical images come with a variety of imaging modalities, each possessing distinct image attributes, intensity profiles, and noise patterns. To reduce the modeling difficulty, we introduce a modality prior for each imaging modality. Similar to the task prior, we initialize a modality prior pool $\mathbf{p}_{\mathcal{M}} \in \mathbb{R}^{|\mathcal{M}| \times l \times C}$, where l denotes the length of the token, and C is the dimension of each token. We employ multiple tokens of length l for each modality. When an image with modality m_k is processed, we select the corresponding modality prior token $\mathbf{p}_{m_k} \in \mathbb{R}^{l \times C}$ and concatenate it with the task prior tokens: $\mathbf{p} = [\mathbf{p}_{t_k}, \mathbf{p}_{m_k}] \in \mathbb{R}^{(|t_k|+l) \times C}$. We then process \mathbf{p} with the prior fusion module.

Hierarchical modeling. The effectiveness of hierarchical modeling is well-established in dense prediction tasks [32, 5]. Drawing inspiration from this, we apply our context prior approach hierarchically at each scale. The posterior prototypes from each scale are concatenated together and processed by an MLP as the final prototypes for segmentation. This design allows Hermes to learn prior knowledge across different scales, effectively merging multi-scale contextual information to improve the segmentation performance.

Algorithm 1 Hermes Training

```

1: Input: Training dataset  $\mathcal{D} = \cup_{k=1}^K \mathcal{D}_k$ , where  $\mathcal{D}_k = \{(\mathbf{x}_k^i, \mathbf{y}_k^i, m_k^i, \mathbf{t}_k^i)\}_{i=1}^{N_k}$ . Randomly initialized
   segmentation backbone  $f_{\theta}$ , task and modality prior pool  $\mathbf{p}_{\mathcal{T}}$  and  $\mathbf{p}_{\mathcal{M}}$ 
2: while not converged do
3:   for j in [1, 2, ..., batch size] do
4:     Randomly choose a training sample  $\mathbf{x}, \mathbf{y}$  from  $\mathcal{D}$ 
5:     Select task and modality priors from the pool:  $\mathbf{p}_t$  and  $\mathbf{p}_m$  according to the oracle:  $\mathbf{t}$  and  $m$ 
6:     Concatenate the priors:  $\mathbf{p} = [\mathbf{p}_t, \mathbf{p}_m]$ 
7:   end for
8:   Assemble the training mini-batch  $\mathcal{B}$ 
9:   Predict the segmentation output:  $P(\hat{\mathbf{y}}|\mathbf{x}, \mathbf{p}) = f_{\theta}(\mathbf{x}, \mathbf{p})$ 
10:  Compute the loss:  $L_{bce}(\mathbf{y}, \hat{\mathbf{y}}) + \lambda L_{dice}(\mathbf{y}, \hat{\mathbf{y}})$ 
11:  Update  $f_{\theta}$ ,  $\mathbf{p}_{\mathcal{T}}$  and  $\mathbf{p}_{\mathcal{M}}$ 
12: end while

```

Training strategy. We leverage a joint training strategy for Hermes to efficiently manage diverse training datasets (refer to Algorithm 1). We use mixed batch training that includes samples from multiple datasets within a training mini-batch. Learning proceeds by minimizing the combination of binary cross-entropy and Dice loss :

$$L(\mathbf{x}, \mathbf{y}, \theta, \mathbf{p}) = L_{bce}(\mathbf{y}, \hat{\mathbf{y}}) + \lambda L_{dice}(\mathbf{y}, \hat{\mathbf{y}}). \quad (3)$$

The backbone and two types of prior tokens are jointly optimized to synergize feature representation learning and context prior knowledge learning.

4 Experiments and Results

4.1 Experiments setup

Dataset selection and experiments design. In Table 1, we have carefully curated a collective training dataset from seven public datasets. We select datasets from three key dimensions, including body region, modality, and clinical targets, allowing us to analyze their impacts under the universal segmentation paradigm. To measure model scalability, we investigate the impact of model size on performance under both traditional training and universal segmentation paradigms. In addition, the upstream multi-task training encourages the model to learn generalizable representations. Therefore, we further evaluate Hermes’ capability under the settings of transfer learning, incremental learning and generalization with two additional datasets.

Table 1: Datasets statistics. The upper datasets are for upstream training and analysis. The bottom two datasets are for downstream tasks on transfer learning, incremental learning, and generalization.

Dataset	Body Region	Modality	Clinical Target	#Cls	Size
BCV [30]	Abdomen	CT	Organs	13	30
LiTS [2]	Abdomen	CT	Liver & Tumor	2	131
KiTS [22]	Abdomen	CT	Kidney & Tumor	2	210
AMOS CT [25]	Abdomen	CT	Organs	15	300
StructSeg [31]	Thorax	CT	Organs	6	50
AMOS MR [25]	Abdomen	MRI	Organs	13	60
CHAOS [27]	Abdomen	T1 & T2 MRI	Organs	4	60
SegTHOR [29]	Thorax	CT	Organs	3	40
MSD Pancreas [1]	Abdomen	CT	Pancreas & Tumor	2	281

Table 2: Universal segmentation results measured with Dice score (%). The upper table presents models with CNN backbones. The lower table shows models with Transformer backbones. Hermes-R denotes our method using ResUNet backbone, while Hermes-M uses MedFormer backbone.

Paradigm	Model	BCV	StructSeg	LiTS Tumor	KiTS Tumor	AMOS CT	AMOS MR	CHAOS	AVG
Traditional	nnUNet [24]	84.23	88.53	64.91	81.72	88.79	85.49	91.34	83.57
Traditional	ResUNet	84.36	88.59	64.87	81.89	88.97	85.43	91.41	83.64
Universal	Hermes-R	85.78	89.43	67.66	85.26	89.59	86.70	92.02	85.20
Traditional	SwinUNETR [18]	83.32	88.36	64.82	74.32	88.29	83.97	88.34	81.63
Traditional	MedFormer [16]	84.61	89.04	66.24	82.09	89.45	85.58	91.85	84.12
Universal	Hermes-M	86.23	89.57	68.55	85.47	89.72	87.15	92.14	85.54

Standardized preprocessing. Training with diverse and heterogeneous data is a non-trivial problem. To address these, we implement a standardized preprocessing pipeline for all datasets. Firstly, we align all images to the same coordinate system and resample the spacing to a uniform $1.5 \times 1.5 \times 1.5 \text{ mm}$. Subsequently, we normalize image intensities; for CT data, we employ a clipping window of [-990, 500], while for MR data, we clip at the 2nd and 98th percentiles of the intensity distribution. Finally, we conduct z-score normalization on each image, ensuring that all data exhibits a zero mean and unit standard deviation.

Implementation details. We implement Hermes using PyTorch and train the model with a batch size of 16 over 200 epochs. We use the LAMB [50] optimizer with a learning rate of 0.002 and an exponential learning rate decay. Data augmentations, including random cropping, rotation, scaling, brightness, contrast, and gamma perturbation, are applied on the fly during training. We use a patch size of $128 \times 128 \times 128$ for 3D training. For the hierarchical modeling, we apply the context prior learning method at the scales of $4 \times$, $8 \times$, and $16 \times$ down-sampling. Given the variation in annotation styles across datasets, we treat classes with identical names in different datasets as unique ROIs, excluding AMOS CT and AMOS MR. This results in 42 task prior tokens. We treat different MRI sequences as a single modality, yielding two total modalities (CT and MRI) in the modality prior pool, where the length l is set as 10. We set $\lambda = 1$ for the loss function. In the upstream training, we randomly divide each of the seven datasets into 80% for training and 20% for evaluation.

4.2 Results

We start initial experiments under the traditional training paradigm by training individual models for each dataset. We use several representative medical image segmentation backbones. For CNN models, we use nnUNet [24] and UNet [43] with residual building blocks [20]: ResUNet. For Transformer models, we use SwinUNETR [18] and MedFormer [16]. From Table 2, ResUNet and MedFormer demonstrate slightly better results under the traditional paradigm. Therefore, in subsequent experiments under the universal paradigm, we employ ResUNet and MedFormer as representative backbones for CNN and Transformer to implement Hermes, i.e. Hermes-R and Hermes-M.

Results on various target ROIs, body regions, and image modalities. To answer the questions raised in the introduction, we analyzed the results of models with the same backbone, i.e. Hermes-R vs ResUNet or Hermes-M vs MedFormer. From Table 2, we see that:

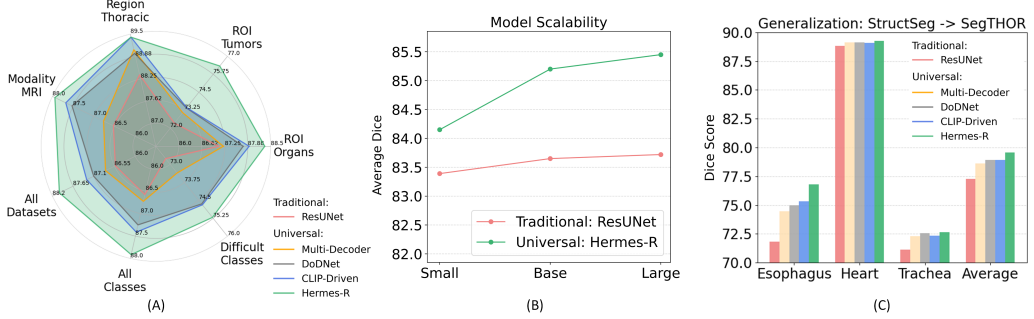


Figure 3: (A) Comparison with other methods. ROIs with Dice score lower than 80 under the traditional paradigm are defined as 'difficult classes'. (B) Model scalability analysis. We scale ResUNet down and up to three variants: ResUNet-Small (10.1M), ResUNet-Base (40.6M), and ResUNet-Large (157.9M), and the same for Hermes. All other experiments use ResUNet-Base as the backbone unless specified. (C) Generalization from StructSeg to SegTHOR.

First, distinct target ROIs mutually boost each other's performance. For instance, Hermes-R yields notable gains over ResUNet for two types of tumor in the LiTS and KiTS datasets, with increments of 2.79% and 3.37%, respectively. In all other ROIs across the seven datasets, Hermes consistently elevates performance, with Hermes-R outperforming ResUNet by 1.56% and Hermes-M surpassing MedFormer by 1.42%. **Second**, the transferability of underlying representations between different body regions is evident. Among the seven datasets, StructSeg is the sole dataset containing thoracic images, while the rest samples are abdominal. Nevertheless, Hermes-R enhances thoracic target segmentation in StructSeg by 0.81% compared to ResUNet, and Hermes-M is 0.53% higher than MedFormer. This suggests that despite anatomical differences, tasks in the abdomen region can contribute to thoracic target segmentation. **Third**, the commonality between imaging modalities can be harnessed to enhance performance, even though they possess entirely different visual characteristics. For instance, AMOS MR is an MRI dataset; CHAOS contains T1 & T2 weighted MRIs, while all other datasets contain CT images. Despite the inherent image differences between these MRI and CT datasets, remarkable improvements are achieved under our universal training paradigm. Specifically, Hermes-R exhibits improvements of 1.27% and 0.61%, and Hermes-M shows gains of 1.57% and 0.29% on AMOS MR and CHAOS, respectively.

Comparison with other methods. We adapt and extend prior methods under the proposed universal segmentation. Multi-decoder [6] uses a shared encoder and separate decoders per dataset. DoDNet [51] was originally designed for organ and tumor segmentation in CT images; we broaden it into multi-organ and multi-modality segmentation. CLIP-Driven [34] was intended for partially labeled CT image analysis; we adapt it by including modality information in its text prompt: "A CT/MRI of a /CLS/." All methods were implemented using the same ResUNet backbone for fairness.

Figure 3 (A) presents a comprehensive comparison of traditional and universal paradigms from seven perspectives. All universal-trained methods demonstrate consistent improvement over the traditional paradigm, particularly for difficult classes, underscoring the universal paradigm's potency in deriving robust representations. Under the universal paradigm, Hermes outperforms other methods in a variety of task perspectives. For example, Multi-Decoder's scalability is limited by the linear growth of decoders with dataset quantity, and it only allows knowledge sharing at the encoder level. DoDNet's one-hot encoding inadequately captures the complex inter-task relationships. CLIP-Driven, despite incorporating knowledge from text prompts, can't effectively encode discriminative information for medical tasks, as its CLIP text encoder lacks training on medical texts, leading to subpar performance, especially for tumors. By contrast, Hermes possesses two key advances by (1) utilizing versatile context priors learned directly from medical data with its shared backbone, and (2) working compatible to a large-scale universal paradigm.

Model scalability. In Figure 3 (B), we find that increasing the model scale yields marginal performance gain in the traditional paradigm. This lack of scalability, in contrast to the notable performance boost seen with larger models in vision tasks [20, 12, 35], is likely due to the limited diversity and volume of data in each individual dataset. The limited data from the same distribution cannot fully utilize the larger model's capacity, potentially leading to overfitting. Contrastingly, the universal

Table 3: Transfer and incremental learning on the MSD Pancreas & Tumor [1] dataset

Setting	Model	1%		10%		50%		100%	
		Pan	Tumor	Pan	Tumor	Pan	Tumor	Pan	Tumor
Scratch	ResUNet	44.60	7.67	74.47	23.90	78.89	44.52	80.45	51.06
	ResUNet (AMOS CT)	56.08	8.31	77.15	25.53	80.53	46.16	81.23	52.21
Transfer	ResUNet (KiTS)	52.68	9.28	75.11	27.33	79.07	45.72	79.23	50.64
	DoDNet	65.48	11.29	76.31	30.00	80.71	47.52	81.32	53.41
	CLIP-Driven	66.25	11.61	77.26	32.18	80.98	48.77	81.35	54.73
Incremental	Hermes-R	72.50	15.46	78.59	42.22	81.00	54.60	82.44	60.83
	DoDNet	63.86	6.32	65.68	13.26	67.75	19.7	67.57	20.32
	CLIP-Driven	71.87	10.41	75.23	22.54	75.8	29.06	75.94	30.17
Incremental	Hermes-R	72.22	13.12	76.36	27.57	78.94	41.72	79.39	45.75

paradigm shifts this dynamic, with an increased backbone scale for Hermes leading to a remarkable performance gain. This finding suggests the proposed universal paradigm’s ability to harness the potential of larger models with diverse data and tasks. It enables the further training of large-scale medical imaging models, as opposed to traditional paradigms with a difficulty to scale up models.

4.3 Downstream task analysis

In the proposed universal training paradigm, the upstream multi-task training encourages the models to learn robust and generalizable representations across various tasks. We extend to perform in-depth analysis on several downstream tasks in the following section.

Transfer learning. We perform evaluation on the challenging MSD pancreas & tumor dataset [1], divided into training (214 samples), validation (10 samples), and testing (57 samples) sets. To assess the influence of downstream data volume, models are fine-tuned on 1%, 10%, 50%, and 100% of the training samples. We report average Dice over 5 runs for the 1% (2 samples) and 10% (21 samples) settings to reduce variability from the training samples.

In Table 3, we provide insights into transfer learning by comparing the performance of different upstream pretraining methods. Compared to the training from scratch, pretraining under traditional single-dataset with AMOS CT (15 organs) or KiTS (kidney & tumor) show improved performance when a small amount of downstream data (1%-10%) is used. However, the performance gains saturate as the volume of downstream task data increases (50%-100%). Notably, KiTS pretraining even underperforms training from scratch when 100% of downstream data is used. In contrast, the improvements offered by the universal paradigm, including DoDNet, CLIP-Driven, and Hermes, are substantial. Particularly, our proposed Hermes achieves significant improvements under both limited (1%-10%) and abundant (50%-100%) downstream data settings. These findings highlight the merit of the universal medical image segmentation paradigm, suggesting that enhanced upstream task diversity could boost transfer learning in downstream tasks.

Incremental learning. We test model performance in a more challenging scenario that requires the model to retain knowledge from previous tasks while learning new ones. For all three compared methods, incremental learning is accomplished by keeping the backbone fixed and finetuning only the new task conditions. From Table 3, Hermes stands out by delivering superior performance under very limited data conditions (1%-10%), even exceeding the transfer learning results from AMOS CT or KiTS. When prepared with an abundance of data, Hermes’ performance remains competitive with that of full model tuning. This incremental learning ability of Hermes emphasizes the strength of the backbone learned during the diverse upstream universal training, leading to support for new downstream medical tasks.

Generalization. We directly apply models trained on the StructSeg to the SegTHOR datasets, both of which contain thoracic CT scans, and evaluate the performance on three overlapping categories as seen in Figure 3 (C). Compared to ResUNet based on the single-dataset training, all three methods trained under the universal paradigm show better generalization, with Hermes leading the performance. This outcome suggests that even with StructSeg being the only thoracic data in our upstream universal training, the inclusion of diverse data types enhances potential generalization capabilities.

4.4 Ablation study

We conducted ablation studies using the ResUNet-Small backbone with Hermes to assess the impact of various configurations. We start with Hermes with only the task prior applied on the $16\times$ down-sampled scale, which is the most basic configuration of our method.

Hierarchically integrating the task priors at multiple scales (e.g., $4\times$, $8\times$, and $16\times$) enhances the average Dice from 82.47% to 83.76%. In the prior fusion module, we employ a bidirectional attention mechanism to concurrently update both the prior and image features. To evaluate the effectiveness of this design, we alter the bidirectional attention to a unidirectional cross-attention. This modification only allows the prior to aggregate information while keeping the image features unchanged, similar to dynamic kernel approaches, e.g. [51, 52]. This change leads to a decrease in the Dice from 83.76% to 82.37%. Incorporating modality priors further improved the model’s capacity to handle complex, heterogeneous multi-modality data, increasing the Dice score from 83.76% to 84.15%.

Table 4: Ablation study

Design	Avg Dice
Task prior only single scale	82.47
Task prior only + hierarchy	83.76
Task prior only - unidirectional fusion	82.37
Task + modality priors	84.15

5 Discussion

Potential impact of the universal medical image segmentation paradigm. Human anatomical structures, despite their wide-ranging visual attributes, possess shared components such as tissues, organs, bones, and muscles [40]. In parallel, different imaging modalities present unique signal representations of the same objects [3]. Drawing from this insight, the rationale of the universal paradigm is to foster learning these commonalities and achieve generalizable representation, particularly helpful for dealing with rare corner cases. Compared with traditional task-specific models, our universal training paradigm can deftly manage an array of clinical tasks. For example, following this paradigm, Hermes incorporates task and modality priors to enable strong flexibility for handling different ROIs and image modalities.

The proposed universal paradigm provides a cost-efficient training approach to building foundational models in medical imaging. The profound challenge in constructing such models lies in data acquisition and aggregation; collecting medical images and fine-grained annotations demands excessive expertise and resources. Creating a large-scale, fully-annotated medical imaging dataset from scratch is exceedingly difficult. To respond this, the proposed universal paradigm can integrate diverse, partially annotated datasets with different clinical targets, even those with conflicting definitions, to train a universal segmentation model with a low cost. This approach can be aligned with the clinical diagnostic workflows, allowing any accessible datasets with different annotation labels to be incorporated into the training process. As a result, our approach offers a reasonable path forward in the development of robust medical imaging foundational models.

Connection with natural image foundation model. Advancements in recent foundational segmentation models (e.g., Segment-Anything Model (SAM) [28]) have demonstrated notable progress for general vision tasks. Yet they have struggled to transfer to medical imaging tasks. For instance, a benchmark study [21] comparing SAM against 12 medical imaging tasks revealed that SAM’s Dice scores consistently fell behind those of UNet by margins ranging from 0.1 to 0.5, and even reaching up to 0.6-0.7. Efforts of finetuning SAM have been made to enhance its medical-image performance (e.g. MedSAM [36]). Despite improvements over SAM, MedSAM’s performance remains inferior to that of our 3D ResUNet baseline, even when the latter is trained from scratch with a single dataset. For example, on CT liver: ResUNet: 97.64 vs. MedSAM: 91.42, and CT pancreas: ResUNet: 80.45 vs. MedSAM: 76.76. The underperformance of SAM in medical imaging tasks may originate from the substantial domain gap [41] and its inherent 2D design, which is ill-equipped to fully harness the 3D information that is crucial to medical image tasks. Therefore, we believe that a foundation model for 3D medical images should be deeply rooted in 3D medical imaging itself. Nevertheless, the proposed universal medical image segmentation paradigm, along with Hermes, offers a versatile means for utilizing diverse, large-scale medical image datasets, opening up perspectives for the development of foundational models in medical imaging.

Future work. While our model effectively leverages the partially labeled data, its performance can be potentially improved by addressing missing labels from self-supervised [19] or semi-supervised learning [47, 46]. We also plan to incorporate more diverse datasets into training, such as additional anatomical regions and imaging modalities. Furthermore, integrating more types of medical prior knowledge into model inference presents an intriguing topic for future investigation.

6 Conclusion

We have introduced a universal medical image segmentation paradigm that learns generalizable and transferable representations from diverse medical image tasks, spanning different targets, body parts, and modalities. Following this training paradigm, we also propose Hermes, an oracle-guided context-prior learning approach, to tackle multiple challenges regarding annotation labeling and image signal heterogeneity. Hermes is able to deal with multiple tasks by harnessing their synergy via our proposed task priors. Meanwhile, the introduced modality prior can remarkably mitigate the difficulties imposed by the heterogeneous imaging modalities. Extensive experiments with Hermes underscore the superiority of this universal paradigm in both upstream and downstream tasks.

References

- [1] Michela Antonelli, Annika Reinke, Spyridon Bakas, Keyvan Farahani, Annette Kopp-Schneider, Bennett A Landman, Geert Litjens, Bjoern Menze, Olaf Ronneberger, Ronald M Summers, et al. The medical segmentation decathlon. *Nature communications*, 13(1):4128, 2022.
- [2] Patrick Bilic, Patrick Ferdinand Christ, Eugene Vorontsov, Grzegorz Chlebus, Hao Chen, Qi Dou, Chi-Wing Fu, Xiao Han, Pheng-Ann Heng, Jürgen Hesser, et al. The liver tumor segmentation benchmark (lits). *arXiv preprint arXiv:1901.04056*, 2019.
- [3] William E Brant and Clyde A Helms. Fundamentals of diagnostic radiology. 2012.
- [4] Tom Brown, Benjamin Mann, Nick Ryder, Melanie Subbiah, Jared D Kaplan, Prafulla Dhariwal, Arvind Neelakantan, Pranav Shyam, Girish Sastry, Amanda Askell, et al. Language models are few-shot learners. *Advances in neural information processing systems*, 33:1877–1901, 2020.
- [5] Liang-Chieh Chen, Yukun Zhu, George Papandreou, Florian Schroff, and Hartwig Adam. Encoder-decoder with atrous separable convolution for semantic image segmentation. In *Proceedings of the European conference on computer vision (ECCV)*, pages 801–818, 2018.
- [6] Sihong Chen, Kai Ma, and Yefeng Zheng. Med3d: Transfer learning for 3d medical image analysis. *arXiv preprint arXiv:1904.00625*, 2019.
- [7] Bowen Cheng, Ishan Misra, Alexander G Schwing, Alexander Kirillov, and Rohit Girdhar. Masked-attention mask transformer for universal image segmentation. In *Proceedings of the IEEE/CVF Conference on Computer Vision and Pattern Recognition*, pages 1290–1299, 2022.
- [8] Bowen Cheng, Alex Schwing, and Alexander Kirillov. Per-pixel classification is not all you need for semantic segmentation. *Advances in Neural Information Processing Systems*, 34:17864–17875, 2021.
- [9] Damai Dai, Yutao Sun, Li Dong, Yaru Hao, Zhifang Sui, and Furu Wei. Why can gpt learn in-context? language models secretly perform gradient descent as meta optimizers. *arXiv preprint arXiv:2212.10559*, 2022.
- [10] Jeffrey De Fauw, Joseph R Ledsam, Bernardino Romera-Paredes, Stanislav Nikolov, Nenad Tomasev, Sam Blackwell, Harry Askham, Xavier Glorot, Brendan O’Donoghue, Daniel Visentin, et al. Clinically applicable deep learning for diagnosis and referral in retinal disease. *Nature medicine*, 24(9):1342–1350, 2018.
- [11] Konstantin Dmitriev and Arie E Kaufman. Learning multi-class segmentations from single-class datasets. In *Proceedings of the IEEE/CVF Conference on Computer Vision and Pattern Recognition*, pages 9501–9511, 2019.
- [12] Alexey Dosovitskiy, Lucas Beyer, Alexander Kolesnikov, Dirk Weissenborn, Xiaohua Zhai, Thomas Unterthiner, Mostafa Dehghani, Matthias Minderer, Georg Heigold, Sylvain Gelly, et al. An image is worth 16x16 words: Transformers for image recognition at scale. *arXiv preprint arXiv:2010.11929*, 2020.
- [13] Chelsea Finn, Pieter Abbeel, and Sergey Levine. Model-agnostic meta-learning for fast adaptation of deep networks. In *International conference on machine learning*, pages 1126–1135. PMLR, 2017.

[14] Yunhe Gao, Rui Huang, Ming Chen, Zhe Wang, Jincheng Deng, Yuanyuan Chen, Yiwei Yang, Jie Zhang, Chanjuan Tao, and Hongsheng Li. Focusnet: Imbalanced large and small organ segmentation with an end-to-end deep neural network for head and neck ct images. In *Medical Image Computing and Computer Assisted Intervention–MICCAI 2019: 22nd International Conference, Shenzhen, China, October 13–17, 2019, Proceedings, Part III 22*, pages 829–838. Springer, 2019.

[15] Yunhe Gao, Rui Huang, Yiwei Yang, Jie Zhang, Kainan Shao, Changjuan Tao, Yuanyuan Chen, Dimitris N Metaxas, Hongsheng Li, and Ming Chen. Focusnetv2: Imbalanced large and small organ segmentation with adversarial shape constraint for head and neck ct images. *Medical Image Analysis*, 67:101831, 2021.

[16] Yunhe Gao, Mu Zhou, Di Liu, Zhennan Yan, Shaoting Zhang, and Dimitris N Metaxas. A data-scalable transformer for medical image segmentation: architecture, model efficiency, and benchmark. *arXiv preprint arXiv:2203.00131*, 2022.

[17] Yunhe Gao, Mu Zhou, and Dimitris N Metaxas. Utnet: a hybrid transformer architecture for medical image segmentation. In *Medical Image Computing and Computer Assisted Intervention–MICCAI 2021: 24th International Conference, Strasbourg, France, September 27–October 1, 2021, Proceedings, Part III 24*, pages 61–71. Springer, 2021.

[18] Ali Hatamizadeh, Vishwesh Nath, Yucheng Tang, Dong Yang, Holger R Roth, and Daguang Xu. Swin unetr: Swin transformers for semantic segmentation of brain tumors in mri images. In *Brainlesion: Glioma, Multiple Sclerosis, Stroke and Traumatic Brain Injuries: 7th International Workshop, BrainLes 2021, Held in Conjunction with MICCAI 2021, Virtual Event, September 27, 2021, Revised Selected Papers, Part I*, pages 272–284. Springer, 2022.

[19] Kaiming He, Xinlei Chen, Saining Xie, Yanghao Li, Piotr Dollár, and Ross Girshick. Masked autoencoders are scalable vision learners. In *Proceedings of the IEEE/CVF Conference on Computer Vision and Pattern Recognition*, pages 16000–16009, 2022.

[20] Kaiming He, Xiangyu Zhang, Shaoqing Ren, and Jian Sun. Deep residual learning for image recognition. In *Proceedings of the IEEE conference on computer vision and pattern recognition*, pages 770–778, 2016.

[21] Sheng He, Rina Bao, Jingpeng Li, P Ellen Grant, and Yangming Ou. Accuracy of segment-anything model (sam) in medical image segmentation tasks. *arXiv preprint arXiv:2304.09324*, 2023.

[22] Nicholas Heller, Niranjan Sathianathan, Arveen Kalapara, Edward Walczak, Keenan Moore, Heather Kaluzniak, Joel Rosenberg, Paul Blake, Zachary Rengel, Makinna Oestreich, et al. The kits19 challenge data: 300 kidney tumor cases with clinical context, ct semantic segmentations, and surgical outcomes. *arXiv preprint arXiv:1904.00445*, 2019.

[23] Rui Huang, Yuanjie Zheng, Zhiqiang Hu, Shaoting Zhang, and Hongsheng Li. Multi-organ segmentation via co-training weight-averaged models from few-organ datasets. In *Medical Image Computing and Computer Assisted Intervention–MICCAI 2020: 23rd International Conference, Lima, Peru, October 4–8, 2020, Proceedings, Part IV 23*, pages 146–155. Springer, 2020.

[24] Fabian Isensee, Paul F Jaeger, Simon AA Kohl, Jens Petersen, and Klaus H Maier-Hein. nnu-net: a self-configuring method for deep learning-based biomedical image segmentation. *Nature methods*, 18(2):203–211, 2021.

[25] Yuanfeng Ji, Haotian Bai, Jie Yang, Chongjian Ge, Ye Zhu, Ruimao Zhang, Zhen Li, Lingyan Zhang, Wanling Ma, Xiang Wan, et al. Amos: A large-scale abdominal multi-organ benchmark for versatile medical image segmentation. *arXiv preprint arXiv:2206.08023*, 2022.

[26] Menglin Jia, Luming Tang, Bor-Chun Chen, Claire Cardie, Serge Belongie, Bharath Hariharan, and Ser-Nam Lim. Visual prompt tuning. In *Computer Vision–ECCV 2022: 17th European Conference, Tel Aviv, Israel, October 23–27, 2022, Proceedings, Part XXXIII*, pages 709–727. Springer, 2022.

[27] A. Emre Kavur, N. Sinem Gezer, Mustafa Barış, Sinem Aslan, Pierre-Henri Conze, Vladimir Groza, Duc Duy Pham, Soumick Chatterjee, Philipp Ernst, Savaş Özkan, Bora Baydar, Dmitry Lachinov, Shuo Han, Josef Pauli, Fabian Isensee, Matthias Perkonigg, Rachana Sathish, Ronnie Rajan, Debdoot Sheet, Gurbandurdy Dovletov, Oliver Speck, Andreas Nürnberger, Klaus H. Maier-Hein, Gözde Bozdağı Akar, Gözde Ünal, Oğuz Dicle, and M. Alper Selver. CHAOS Challenge - combined (CT-MR) healthy abdominal organ segmentation. *Medical Image Analysis*, 69:101950, April 2021.

[28] Alexander Kirillov, Eric Mintun, Nikhila Ravi, Hanzi Mao, Chloe Rolland, Laura Gustafson, Tete Xiao, Spencer Whitehead, Alexander C Berg, Wan-Yen Lo, et al. Segment anything. *arXiv preprint arXiv:2304.02643*, 2023.

[29] Zoé Lambert, Caroline Petitjean, Bernard Dubray, and Su Kuan. Segthor: Segmentation of thoracic organs at risk in ct images. In *2020 Tenth International Conference on Image Processing Theory, Tools and Applications (IPTA)*, pages 1–6. IEEE, 2020.

[30] Bennett Landman, Zhoubing Xu, Juan Lgelsias, Martin Styner, Thomas Langerak, and Klein Arno. Multi-atlas labeling beyond the cranial vault - workshop and challenge.

[31] Hongsheng Li, Jinghao Zhou, Jincheng Deng, and Ming Chen. Automatic structure segmentation for radiotherapy planning challenge 2019.

[32] Tsung-Yi Lin, Piotr Dollár, Ross Girshick, Kaiming He, Bharath Hariharan, and Serge Belongie. Feature pyramid networks for object detection. In *Proceedings of the IEEE conference on computer vision and pattern recognition*, pages 2117–2125, 2017.

[33] Jiachang Liu, Dinghan Shen, Yizhe Zhang, Bill Dolan, Lawrence Carin, and Weizhu Chen. What makes good in-context examples for gpt-3? *arXiv preprint arXiv:2101.06804*, 2021.

[34] Jie Liu, Yixiao Zhang, Jie-Neng Chen, Junfei Xiao, Yongyi Lu, Bennett A Landman, Yixuan Yuan, Alan Yuille, Yucheng Tang, and Zongwei Zhou. Clip-driven universal model for organ segmentation and tumor detection. *arXiv preprint arXiv:2301.00785*, 2023.

[35] Ze Liu, Yutong Lin, Yue Cao, Han Hu, Yixuan Wei, Zheng Zhang, Stephen Lin, and Baining Guo. Swin transformer: Hierarchical vision transformer using shifted windows. In *Proceedings of the IEEE/CVF international conference on computer vision*, pages 10012–10022, 2021.

[36] Jun Ma and Bo Wang. Segment anything in medical images. *arXiv preprint arXiv:2304.12306*, 2023.

[37] Sewon Min, Mike Lewis, Luke Zettlemoyer, and Hannaneh Hajishirzi. Metaicl: Learning to learn in context. *arXiv preprint arXiv:2110.15943*, 2021.

[38] Sewon Min, Xinxin Lyu, Ari Holtzman, Mikel Artetxe, Mike Lewis, Hannaneh Hajishirzi, and Luke Zettlemoyer. Rethinking the role of demonstrations: What makes in-context learning work? *arXiv preprint arXiv:2202.12837*, 2022.

[39] Ursula Nestle, Stephanie Kremp, Andrea Schaefer-Schuler, Christiane Sebastian-Welsch, Dirk Hellwig, Christian Rübe, and Carl-Martin Kirsch. Comparison of different methods for delineation of 18f-fdg pet-positive tissue for target volume definition in radiotherapy of patients with non-small cell lung cancer. *Journal of nuclear medicine*, 46(8):1342–1348, 2005.

[40] Frank H Netter. *Atlas of human anatomy, Professional Edition E-Book: including NetterReference.com Access with full downloadable image Bank*. Elsevier health sciences, 2014.

[41] Maithra Raghu, Chiyuan Zhang, Jon Kleinberg, and Samy Bengio. Transfusion: Understanding transfer learning for medical imaging. *Advances in neural information processing systems*, 32, 2019.

[42] Muhammad Imran Razzak, Saeeda Naz, and Ahmad Zaib. Deep learning for medical image processing: Overview, challenges and the future. *Classification in BioApps: Automation of Decision Making*, pages 323–350, 2018.

[43] Olaf Ronneberger, Philipp Fischer, and Thomas Brox. U-net: Convolutional networks for biomedical image segmentation. In *Medical Image Computing and Computer-Assisted Intervention–MICCAI 2015: 18th International Conference, Munich, Germany, October 5–9, 2015, Proceedings, Part III 18*, pages 234–241. Springer, 2015.

[44] Sebastian Ruder. An overview of multi-task learning in deep neural networks. *arXiv preprint arXiv:1706.05098*, 2017.

[45] Wei Shen, Mu Zhou, Feng Yang, Caiyun Yang, and Jie Tian. Multi-scale convolutional neural networks for lung nodule classification. In *Information Processing in Medical Imaging: 24th International Conference, IPMI 2015, Sabhal Mor Ostaig, Isle of Skye, UK, June 28–July 3, 2015, Proceedings 24*, pages 588–599. Springer, 2015.

[46] Kihyuk Sohn, David Berthelot, Nicholas Carlini, Zizhao Zhang, Han Zhang, Colin A Raffel, Ekin Dogus Cubuk, Alexey Kurakin, and Chun-Liang Li. Fixmatch: Simplifying semi-supervised learning with consistency and confidence. *Advances in neural information processing systems*, 33:596–608, 2020.

[47] Antti Tarvainen and Harri Valpola. Mean teachers are better role models: Weight-averaged consistency targets improve semi-supervised deep learning results. *Advances in neural information processing systems*, 30, 2017.

[48] Xinlong Wang, Wen Wang, Yue Cao, Chunhua Shen, and Tiejun Huang. Images speak in images: A generalist painter for in-context visual learning. *arXiv preprint arXiv:2212.02499*, 2022.

[49] Sang Michael Xie, Aditi Raghunathan, Percy Liang, and Tengyu Ma. An explanation of in-context learning as implicit bayesian inference. *arXiv preprint arXiv:2111.02080*, 2021.

[50] Yang You, Jing Li, Sashank Reddi, Jonathan Hseu, Sanjiv Kumar, Srinadh Bhojanapalli, Xiaodan Song, James Demmel, Kurt Keutzer, and Cho-Jui Hsieh. Large batch optimization for deep learning: Training bert in 76 minutes. *arXiv preprint arXiv:1904.00962*, 2019.

[51] Jianpeng Zhang, Yutong Xie, Yong Xia, and Chunhua Shen. Dodnet: Learning to segment multi-organ and tumors from multiple partially labeled datasets. In *Proceedings of the IEEE/CVF conference on computer vision and pattern recognition*, pages 1195–1204, 2021.

[52] Wenwei Zhang, Jiangmiao Pang, Kai Chen, and Chen Change Loy. K-net: Towards unified image segmentation. *Advances in Neural Information Processing Systems*, 34:10326–10338, 2021.

[53] Zihao Zhao, Eric Wallace, Shi Feng, Dan Klein, and Sameer Singh. Calibrate before use: Improving few-shot performance of language models. In *International Conference on Machine Learning*, pages 12697–12706. PMLR, 2021.

[54] Yuyin Zhou, Zhe Li, Song Bai, Chong Wang, Xinlei Chen, Mei Han, Elliot Fishman, and Alan L Yuille. Prior-aware neural network for partially-supervised multi-organ segmentation. In *Proceedings of the IEEE/CVF international conference on computer vision*, pages 10672–10681, 2019.

Appendix A Dataset details

In this section, we provide detailed information about each dataset, including the volume of data, annotation categories, data sources, as well as how we use them for training and testing. At last, we explain how we designed our experiments using these datasets.

Table 5: Datasets statistics. The upper datasets are for upstream training and analysis. The bottom two datasets are for downstream tasks on transfer learning, incremental learning, and generalization.

Dataset	Body Region	Modality	Clinical Target	#Cls	Size
BCV [30]	Abdomen	CT	Organs	13	30
LiTS [2]	Abdomen	CT	Liver & Tumor	2	131
KiTS [22]	Abdomen	CT	Kidney & Tumor	2	210
AMOS CT [25]	Abdomen	CT	Organs	15	300
StructSeg [31]	Thorax	CT	Organs	6	50
AMOS MR [25]	Abdomen	MRI	Organs	13	60
CHAOS [27]	Abdomen	T1 & T2 MRI	Organs	4	60
SegTHOR [29]	Thorax	CT	Organs	3	40
MSD Pancreas [1]	Abdomen	CT	Pancreas & Tumor	2	281

BCV dataset. The BCV dataset [30] (Multi-Atlas Labeling Beyond the Cranial Vault) comprises 50 subjects with abdominal CT scans, of which 30 training images are publicly available. Thirteen abdominal organs were manually labeled on a volumetric basis using the MIPAV software. The labeled organs include the spleen, right kidney, left kidney, gallbladder, esophagus, liver, stomach, aorta, inferior vena cava, portal vein and splenic vein, pancreas, right adrenal gland, and left adrenal gland. Some patients may lack the right kidney or gallbladder, and therefore these organs are not labeled. All scans were acquired for routine clinical care from CT scanners at the Vanderbilt University Medical Center (VUMC). The BCV dataset is used as one of the seven datasets for upstream training. We randomly select 80% of the 30 publicly available images for training and 20% for testing.

LiTS dataset. The LiTS dataset [2] (Liver Tumor Segmentation Challenge) comprises 201 computed tomography (CT) images of the abdomen, with 131 training cases and 70 testing cases, where only the label of training cases are publicly available. The LiTS dataset provides detailed annotation for tumors while offering coarse annotation for the liver. The image data originates from various clinical sites, including Ludwig Maximilian University of Munich, Radboud University Medical Center of Nijmegen, Polytechnique & CHUM Research Center Montréal, Tel Aviv University, Sheba Medical Center, IRCAD Institute Strasbourg, and the Hebrew University of Jerusalem. The studied subjects suffer from diverse liver tumor diseases, such as hepatocellular carcinoma (HCC), as well as secondary liver tumors and metastases originating from colorectal, breast, and lung cancers. The tumors exhibit varying contrast enhancement, including hyper and hypo-dense contrast. The images represent a mix of pre- and post-therapy abdominal CT scans, acquired with different CT scanners and acquisition protocols. The LiTS dataset is used as one of the seven datasets for upstream training. We conduct experiments using the 131 training dataset by randomly selecting 80% for training and 20% for testing.

KiTS dataset. The KiTS19 dataset [22] comprises segmented CT imaging and treatment outcomes for 300 patients who underwent partial or radical nephrectomy for one or more kidney tumors at the University of Minnesota Medical Center between 2010 and 2018. Out of these cases, 210 have been released publicly, while the remaining 90 are kept private for evaluation purposes. The KiTS is used as one of the seven datasets for upstream training. We conduct experiments using the 210 scans from the training dataset by randomly selecting 80% for training and 20% for testing.

AMOS CT & MR dataset. The AMOS dataset [25] is a large-scale collection of CT and MRI data from 600 patients diagnosed with abdominal tumors or abnormalities at Longgang District People’s Hospital. The dataset comprises 500 CT and 100 MRI scans acquired from eight different scanners and vendors, encompassing 15 organ categories: spleen, right kidney, left kidney, gallbladder, esophagus, liver, stomach, aorta, inferior vena cava, pancreas, right adrenal gland, left adrenal gland, duodenum, bladder, and prostate/uterus. For CT images, AMOS provides 200 scans for training and 100 scans for validation, while for MRI images, 40 scans are provided for training and 20 scans for validation. Both AMOS CT and AMOS MR are used as two of the seven datasets for upstream training. In line with the AMOS benchmark paper [25], we report performance on the validation set

and utilize all training data for model training. As all images in the AMOS MR validation set don't have the annotation of bladder and prostate, we only segment 13 organs for AMOS MR.

StructSeg dataset. The StructSeg dataset [31] is collected from a challenge for the segmentation of organs-at-risk (OAR) and gross target volume (GTV) of tumors of two types of cancers, nasopharynx cancer and lung cancer, for radiation therapy planning. We use Task 3, organ-at-risk segmentation from chest CT scans in our experiments. Six OARs are annotated on CT scans from 50 lung cancer patients. The six OARs are the left lung, right lung, spinal cord, esophagus, heart, and trachea. The StructSeg dataset is the only thorax dataset for upstream training. We split the 50 scans into 80% training and 20% testing.

CHAOS dataset. The CHAOS dataset [27] is collected from a challenge for the precise segmentation of abdominal organs. We use the data from Task 5: segmentation of abdominal organs from MRI. Four organs, including the liver, left kidney, right kidney, and spleen are annotated. They provide three MR sequences, including T1-in-phase, T1-out-phase, and T2-SPIR, for 20 patients. We treat different MR sequences as separate images and split the dataset at the patient level into 80% training and 20% testing.

SegTHOR dataset. The SegTHOR dataset [29] aims at the thoracic organ-at-risk segmentation in CT images. This dataset provides 4 OARs annotations from 40 CT scans, including heart, aorta, trachea, and esophagus. We use the SegTHOR dataset as a downstream task to evaluate the generalization of models. We directly use the upstream-trained model to make predictions on all 40 images and report the generalization performance.

MSD pancreas & tumor dataset. The MSD pancreas & tumor dataset is a part of the Medical Image Segmentation Decathlon (MSD) [1], an international challenge aimed at identifying a general-purpose algorithm for medical image segmentation. The competition encompasses ten distinct datasets featuring various target regions, modalities, and challenging attributes. MSD pancreas & tumor is one of the datasets that is annotated for pancreas and tumors. The shape and position of tumors vary greatly between patients. The MSD pancreas & tumor dataset consists of 281 CT images. We use it as a downstream task to evaluate models' capacity for transfer learning and incremental learning. We split the dataset into 214 samples for training, 10 samples for validation, and 57 samples for testing. To evaluate the impact of downstream data volume, we conduct experiments on 1%, 10%, 50%, and 100% of the 214 training samples. To reduce the variability from the training sample selection, we report the average performance over 5 runs for the 1% and 10% settings.

Experiment design. To substantiate the efficacy of the proposed universal medical image segmentation paradigm, we have meticulously curated these datasets, see Table 5. These datasets were selected based on three main factors: anatomical regions, imaging modalities, and clinical targets. In terms of anatomical regions, six datasets focused on the abdominal region were incorporated, while StructSeg served as the sole representative for the thoracic region. This selection facilitates to assess the influence of abdominal-focused tasks on thoracic-based tasks. With respect to imaging modalities, our selection covers a range of CT-based tasks, leaving AMOS MR and CHAOS as the datasets with MRI modalities. This particular selection enables us to investigate the potential mutual benefits between CT and MR tasks. As for the clinical targets, our dataset selection includes five organ-specific datasets and two tumor-centric ones. This variance enables a deeper exploration of the interplay between clinical targets that are markedly distinct in terms of both their morphology and appearance. The careful selection of these upstream training datasets is designed to provide comprehensive answers to the three research questions originally posed in our introduction section.

For the downstream tasks, we choose the challenging MSD pancreas & tumor dataset for transfer learning and incremental learning. The pancreas is a relatively small, elongated glandular organ, while the shape and location of a pancreatic tumor can greatly vary. As such, the segmentation difficulty of this task is extremely high. Furthermore, this dataset is comprised of a large number of images, with 281 CT scans, allowing us to adequately test the model's transfer learning and incremental learning abilities under various downstream data volumes.

In addition, we select the SegTHOR dataset to verify the model's generalization performance. There is only one thoracic dataset (StructSeg) in the upstream training. The StructSeg and SegTHOR are both for thoracic OAR segmentation and have three overlap categories of heart, trachea, and esophagus. Evaluating performance on these overlapping categories allows us to explore the universal

paradigm's potential generalization ability to different anatomical regions and analyze whether more abdominal tasks contribute positively to the generalization of thoracic tasks.

Appendix B Supplement method

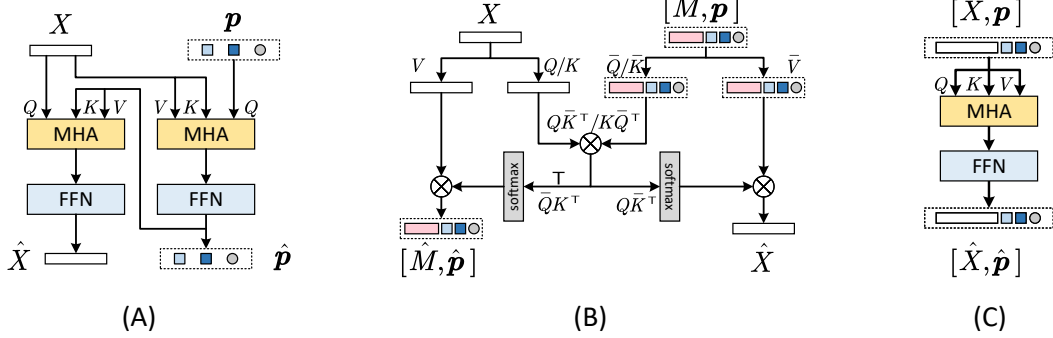


Figure 4: The implementation of prior fusion module for existing backbones. (A) The implementation for CNN backbones, like ResUNet [43]. We use a bi-directional cross-attention module to process both the feature map X and the prior tokens \mathbf{p} . (B) The implementation for MedFormer [16]. We merge the prior tokens into the semantic map of its B-MHA module. (C) The implementation for conventional attention module, e.g. ViT [12] backbone. The normalization layers and residue connections for all three implementations are omitted for simplicity.

B.1 Prior fusion module details

The prior fusion module is an essential part of Hermes, which is responsible for integrating knowledge encapsulated in prior tokens with image feature maps. This fusion process utilizes attention modules, enabling efficient and global information exchange between prior tokens and feature maps. This design ensures Hermes' compatibility with existing backbones. We illustrate several implementations for common backbones in Figure 4. We first introduce the formulation with the conventional attention module. Then, we introduce the bi-directional cross-attention for CNN backbones. Finally, we show how to merge the prior fusion into the MedFormer backbone.

Conventional attention module. Conventional Transformer architectures (e.g. ViT [12]) often rely on multi-head self-attention that captures the all-to-all pairwise dependencies among input tokens. To extend, we present a general formulation of merging prior fusion into a conventional attention module, see Figure 4 (C). Given the input feature map $X \in \mathcal{R}^{n \times C}$ ($n = D \times H \times W$ is the number of tokens in the feature map, C denotes the token dimension), and the prior tokens $\mathbf{p} \in \mathcal{R}^{(|\mathbf{t}_k|+l) \times C}$, where $|\mathbf{t}_k|$ denotes the number of tasks, and l is the length of each modality prior. We first concatenate the feature map and the prior tokens together as the input of the transformer block: $I = [X, \mathbf{p}] \in \mathcal{R}^{n+|\mathbf{t}_k|+l \times C}$. The conventional Transformer block operates as follows:

$$\begin{aligned}
 I' &= \text{LN}(I) \\
 I'' &= \text{MHA}(I', I', I') + I \\
 \text{MHA}(q, k, v) &= [\text{head}_1, \dots, \text{head}_h]W^O \\
 \text{head}_i &= \text{Attention}(qW_i^Q, kW_i^K, vW_i^V) \\
 \text{Attention}(\mathbf{Q}, \mathbf{K}, \mathbf{V}) &= \text{softmax}\left(\frac{\mathbf{Q}\mathbf{K}^T}{\sqrt{d_h}}\right)\mathbf{V} \\
 \hat{I} &= \text{FFN}(\text{LN}(I'')) + I''
 \end{aligned} \tag{4}$$

where W_Q, W^K, W^V, W^O are weight matrices, and d_h is the dimension of each head. We can then obtain the prior-injected feature map and the posterior tokens by splitting $\hat{I} = [\hat{X}, \hat{\mathbf{p}}]$. The computation complexity for the above prior-modified attention module is $O((n + |\mathbf{t}_k| + l)^2)$.

CNN backbones. CNN backbones, like ResUNet [43, 20], usually use hierarchical architectures. The quadratic complexity of the above all-to-all attention makes it unaffordable to apply the prior fusion module on high-resolution feature maps (e.g. $n = 32,768$ for a $32 \times 32 \times 32$ feature map). Therefore, we implement the prior fusion module with a bi-directional cross-attention module instead, see Figure 4 (A). The prior tokens \mathbf{p} first aggregate image-specific information from the feature map X to obtain the posterior tokens $\hat{\mathbf{p}}$:

$$\begin{aligned}\mathbf{p}' &= \text{LN}(\mathbf{p}) \\ X' &= \text{LN}(X) \\ \mathbf{p}'' &= \text{MHA}(\mathbf{p}', X', X') + \mathbf{p} \\ \hat{\mathbf{p}} &= \text{FFN}(\text{LN}(\mathbf{p}'')) + \mathbf{p}''\end{aligned}\tag{5}$$

Then we inject the knowledge in the posterior tokens to obtain the prior-injected feature map \hat{X} :

$$\begin{aligned}\hat{\mathbf{p}}' &= \text{LN}(\hat{\mathbf{p}}) \\ X'' &= \text{MHA}(X', \hat{\mathbf{p}}', \hat{\mathbf{p}}') + X \\ \hat{X} &= \text{FFN}(\text{LN}(X'')) + X''\end{aligned}\tag{6}$$

As $|\mathbf{t}_k| + l \ll n$, the computation complexity of the bi-direction cross-attention for the prior fusion module is $O(n)$. For example, for the dataset with the most tasks, AMOS CT, $|\mathbf{t}_k| + l = 25 \ll n = 32,768$ for a $32 \times 32 \times 32$ feature map. With this design, the prior fusion module can adaptively integrate the prior tokens and the feature maps with minor additional computational costs. We implement Hermes-R by inserting the cross-attention module at the end of each stage of the ResUNet, i.e. after the convolution layers at $4\times, 8\times$, and $16\times$ downsampling scales.

MedFormer. MedFormer [16] is a Transformer model proposed for medical image segmentation. One key component of MedFormer is its B-MHA attention module, which incorporates a compressed semantic map to reduce computation complexity as well as enhance representation learning. In Figure 4 (B), we show our implementation of merging the prior fusion module into the B-MHA module of the MedFormer backbone. In B-MHA, M is a semantic map that is encoded and refined for rich semantic information within a much lower spatial resolution compared to the feature map X . We concatenate the semantic map M with the prior tokens \mathbf{p} : $I_M = [M, \mathbf{p}]$. The X and I_M are linearly projected to $\mathbf{Q}/\mathbf{K}/\mathbf{V}$ and $\bar{\mathbf{Q}}/\bar{\mathbf{K}}/\bar{\mathbf{V}}$ respectively. To reduce the computation, B-MHA shares the query and key of X and I_M , i.e. $\mathbf{Q} = \mathbf{K}$ and $\bar{\mathbf{Q}} = \bar{\mathbf{K}}$, as the dot product of the query and key in cross-attention measures the similarity of token pairs of two inputs, which is symmetrical. The attention matrix is reused by simply transposing the dot product matrix:

$$\begin{aligned}\hat{X} &= \text{Attention}(\mathbf{Q}, \bar{\mathbf{K}}, \bar{\mathbf{V}}) = \text{softmax}\left(\frac{\mathbf{Q}\bar{\mathbf{K}}^\top}{\sqrt{d}}\right)\bar{\mathbf{V}} \\ \hat{I}_M &= \text{Attention}(\bar{\mathbf{Q}}, \mathbf{K}, \mathbf{V}) = \text{softmax}\left(\frac{\bar{\mathbf{Q}}\mathbf{K}^\top}{\sqrt{d}}\right)\mathbf{V} \\ (\mathbf{Q}\bar{\mathbf{K}}^\top)^\top &= (\bar{\mathbf{Q}}\mathbf{K}^\top)^\top = \bar{\mathbf{Q}}\mathbf{K}^\top\end{aligned}\tag{7}$$

The normalization layer, FFN, and residue connections are not included in the equation for simplicity. More details can be found in the original MedFormer paper. We can then obtain the updated semantic map and the posterior tokens by splitting $\hat{I}_M = [\hat{M}, \hat{\mathbf{p}}]$. As $|M| + |\mathbf{t}_k| + l \ll n$, the computation complexity is $O(n)$. We implement Hermes-M by incorporating the prior fusion module with the B-MHA module on the $4\times, 8\times$ and $16\times$ downsampling scales within the MedFormer backbone.

Computation comparison. In Table 6, we present the GPU memory usage, number of parameters, and inference time for Hermes with various backbones. For the ResUNet backbone, thanks to the efficient bi-directional cross-attention, Hermes-R only slightly increases GPU memory usage and inference time, despite additional parameters due to the cross-attention in the prior fusion module. For the Transformer backbone MedFormer, Hermes-M demonstrates almost identical consumption on memory, inference time, and the number of parameters compared with MedFormer. These results exemplify the efficacy of integrating the prior fusion module into MedFormer’s existing

attention module, highlighting Hermes’ ability in leveraging different backbones without significantly impacting the required computational resources.

Table 6: Computation comparison between the Hermes and the corresponding backbone. The memory consumption and inference time are measured with an image size of $2 \times 1 \times 128 \times 128 \times 128$ on one Nvidia A100 GPU. We report the average inference time over 100 runs.

Model	Memory/G	#Params/M	Inference Time/s
ResUNet	11.23	40.56	0.13
Hermes-R	11.54	59.61	0.16
MedFormer	11.44	43.20	0.19
Hermes-M	11.62	44.50	0.20

Appendix C Supplement results

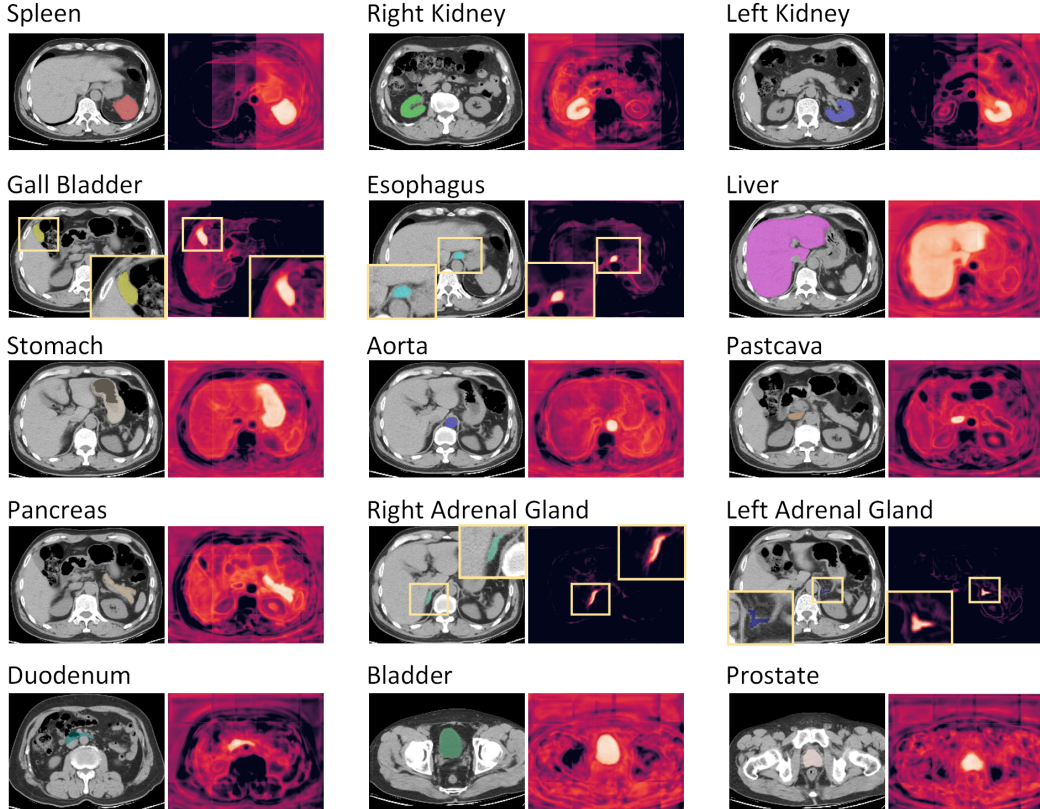


Figure 5: Heatmap visualization of each posterior prototype for the AMOS CT dataset. The brighter means the higher similarity. The yellow boxes are the zoomed-in version of small organs for better visualization.

Visual analysis. In Figure 5, we show the heatmap visualization of each posterior prototype with the output feature map of the decoder measured with dot-product similarity. The visualization underscores the quality of Hermes’s predicted posterior prototypes, which adeptly capture the semantic essence of each category, aligning closely with the respective feature maps. Remarkably, Hermes manages precise predictions even for small organs with complex shapes. Take the right and left adrenal glands as an example: despite their tiny size and irregular shape, the posterior prototypes predicted by Hermes accurately reflect their intricate edges.

Table 7: Comparison with other methods. ResUNet is trained with the traditional paradigm, while all comparison methods are reimplemented with the ResUNet backbone for fair comparison and extend to the universal medical image segmentation paradigm.

Model	BCV	StructSeg	LiTS Tumor	KiTS Tumor	AMOS CT	AMOS MR	CHAOS	AVG
ResUNet	84.36	88.59	64.87	81.89	88.97	85.43	91.41	83.64
Multi-decoder [6]	83.89	89.15	65.82	81.92	89.28	85.61	91.54	83.88
DoDNet [51]	85.16	89.07	65.43	82.83	89.06	86.41	91.53	84.21
CLIP-driven [34]	85.37	89.43	65.42	82.89	89.05	86.47	91.86	84.35
Hermes-R	85.78	89.43	67.66	85.26	89.59	86.70	92.02	85.20

Comparison with other methods. We provide the detailed performance of other comparison methods on each dataset, see Table 7. The ResUNet is trained under the traditional paradigm. All comparison methods are trained with the universal paradigm and are implemented with ResUNet for a fair comparison. All methods under the universal paradigm exhibit better performance compared with traditionally trained ResUNet. Among universal method settings, our Hermes-R shows a consistent advantage on the seven upstream datasets.

Ablation on the length of modality prior token. We present an additional ablation study on the length of the modality prior token, see Table 8. We follow the setting in the ablation study section in the manuscript using the ResUNet-Small backbone to implement Hermes. Given that each modality encompasses a significant amount of variation, we find that a modality prior of length 1 does not possess adequate capacity to encode modality-related information. We observe that longer modality tokens further improve the performance, but the gains saturate as the length increases. Therefore, we choose $l = 10$ for our main experiments.

Table 8: Ablation study on the length of modality prior token. We report the average Dice on the seven datasets with Hermes implemented with the ResUNet-Small backbone.

l	1	5	10	20
Avg Dice	83.83	84.04	84.15	84.17